

Simultaneous Evolution of Uniaxially Oriented Grains and Ultralow-Density Grain-Boundary Network in $\text{CH}_3\text{NH}_3\text{PbI}_3$ Perovskite Thin Films Mediated by Precursor Phase Metastability

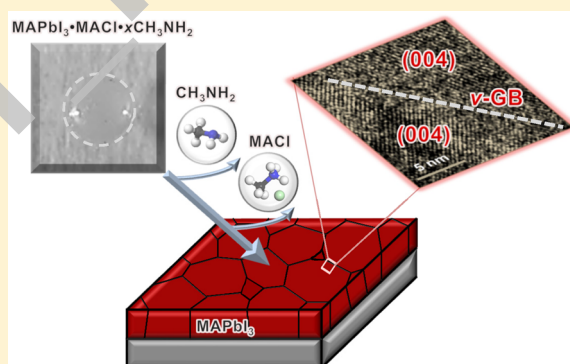
Fuxiang Ji,[†] Shuping Pang,^{*,†,‡} Lin Zhang,[‡] Yingxia Zong,^{†,‡} Guanglei Cui,^{†,‡} Nitin P. Padture,^{*,‡,§} and Yuanyuan Zhou^{*,‡}

[†]Qingdao Institute of Bioenergy and Bioprocess Technology, Chinese Academy of Sciences, 189 Songling Road, Qingdao 266101, PR China

[‡]School of Engineering, Brown University, 184 Hope Street, Providence, Rhode Island 02912, United States

S Supporting Information

ABSTRACT: Solution-processed organic–inorganic halide perovskite (OIHP) thin films typically contain fine, randomly oriented grains and a high-density grain-boundary network, which are unfavorable for key film functions including charge transport and environmental stability. Here, we report a new chemical route for achieving $\text{CH}_3\text{NH}_3\text{PbI}_3$ (MAPbI_3) OIHP thin films comprising large, uniaxially oriented grains and an ultralow-density grain-boundary network. This route starts with a new metastable liquid-state precursor phase, $\text{MAPbI}_3 \cdot \text{MACl} \cdot x\text{CH}_3\text{NH}_2$, which converts to metastable $\text{MAPbI}_3 \cdot \text{MACl}$ and then to MAPbI_3 OIHP upon stepwise release of volatile CH_3NH_2 and MACl . Perovskite solar cells made via this route show high power conversion efficiency of up to 19.4%, with significantly enhanced environmental stability.



Organic–inorganic halide perovskites (OIHPs) have emerged as a new family of semiconductors that hold unprecedented promise as light-absorber materials in solution-processed thin-film solar cells.^{1–5} Owing to the outstanding optoelectronic properties of OIHPs, the rise in the power conversion efficiency (PCE) of perovskite solar cells (PSCs) has been swift. Generally, solution-processed thin films of $\text{CH}_3\text{NH}_3\text{PbI}_3$ (MAPbI_3), the most widely studied OIHP for PSCs,¹ are polycrystalline in nature. Thus, the crystalline grains and the associated grain-boundary (GB) network are the most prominent microstructural features that determine OIHP thin-film properties and consequently the performance of PSCs.^{6,7} It has been recognized that the key characteristics of both, grains (e.g., size, orientation) and GB-network (e.g., density), in the MAPbI_3 thin films have profound effect on the charge-carrier transport properties.^{7–11} It has also been revealed that the GB-network density in the MAPbI_3 film determines the environmental-degradation kinetics of MAPbI_3 ,¹² because GBs are the “weakest” regions where dangling or wrong bonds proliferate.¹³ Because it is extremely challenging to fabricate GB-free, single-crystal MAPbI_3 thin films using solution-based methods,¹¹ there is a pressing need to engineer the grains and the GB-

network in MAPbI_3 thin films in order to achieve desired properties that can approach those of single-crystal thin films. To that end, popular methods such as solvent engineering and annealing, gas-blowing, and additive engineering have been highly successful in achieving uniform MAPbI_3 films with micrometer-sized grains.^{14–18} However, these methods invariably result in grains with random orientations. There have been a few studies involving the control of grain orientation, i.e. texture, in MAPbI_3 films.^{8–10,19} However, this usually results in compromising either the film uniformity or the coarseness of the grains. In this context, previously we have reported a highly scalable deposition method which entails rapid crystallization of highly uniform and textured, but fine-grained MAPbI_3 thin films using an unconventional liquid-phase precursor: $\text{MAPbI}_3 \cdot x\text{CH}_3\text{NH}_2$.^{20–22} This precursor phase is metastable, and it converts to MAPbI_3 OIHP at room temperature (RT) upon rapid CH_3NH_2 self-degassing.^{20–22} This chemical conversion is coupled with high MAPbI_3 nucleation rate, which invariably

Received: October 9, 2017

Accepted: November 3, 2017



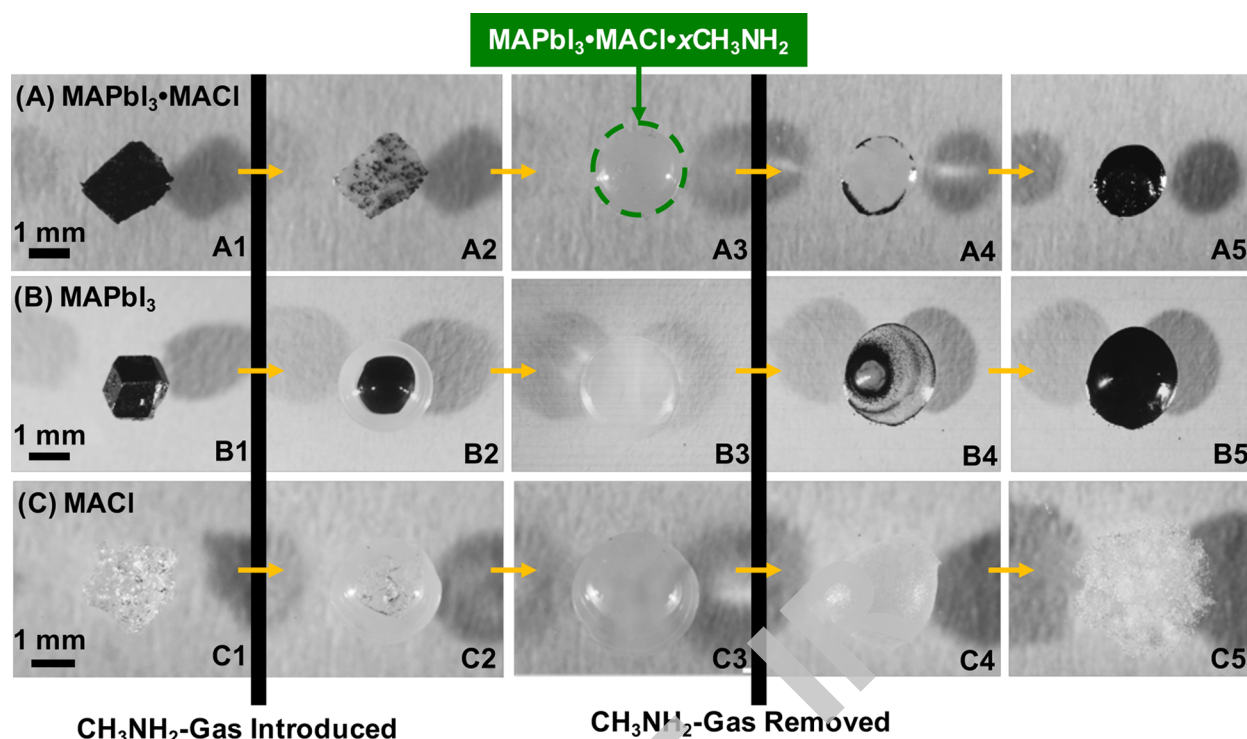


Figure 1. (A) In situ optical microscopy observations showing the formation of metastable $\text{MAPbI}_3 \cdot \text{MACl} \cdot x\text{CH}_3\text{NH}_2$ liquid precursor phase by exposing a $\text{MAPbI}_3 \cdot \text{MACl}$ solid particle to CH_3NH_2 gas at RT and the crystallization of a smooth $\text{MAPbI}_3 \cdot \text{MACl}$ solid particle after the CH_3NH_2 gas is removed at RT. Parallel control experiments with phase-pure solid particles of (B) MAPbI_3 and (C) MACl .

leads to fine grains and high-density GB-network in the final thin film.

In this study, we take advantage of the unique combination of high uniformity and strong texture in MAPbI_3 OIHP thin films produced using this method and introduce a new precursor phase, $\text{MAPbI}_3 \cdot \text{MACl} \cdot x\text{CH}_3\text{NH}_2$, whose metastability can be engineered. The rational addition of MACl is based on the consideration that MACl exists in the solid state at RT but decomposes/sublimes upon annealing at elevated temperatures ($>100^\circ\text{C}$).^{18,23} This new metastable precursor allows stepwise, well-controlled evolution of ultralarge grains (up to ten times the film thickness) with a uniaxial 110 “mosaic” texture and ultralow-density GB-network consisting of only vertical GBs in the final MAPbI_3 OIHP thin films. This exceptional combination of large, textured grains and low-density GB-network leads to enhanced thin-film properties and results in PSCs that have high efficiencies and enhanced environmental stability.

Initially, some “model” experiments were performed on solid particles, where the metastable $\text{MAPbI}_3 \cdot \text{MACl} \cdot x\text{CH}_3\text{NH}_2$ precursor was synthesized by exposing $\text{MAPbI}_3 \cdot \text{MACl}$ solid particles to CH_3NH_2 gas at RT. The $\text{MAPbI}_3 \cdot \text{MACl} \cdot x\text{CH}_3\text{NH}_2$ precursor formation process is revealed using in situ optical microscopy (OM). As seen in Figure 1A (OM images A1–A3), when CH_3NH_2 is introduced, the $\text{MAPbI}_3 \cdot \text{MACl}$ solid particle begins to be bleached heterogeneously, resulting in a colorless particle with embedded black specks. With further CH_3NH_2 exposure, a clear, smooth liquid drop of $\text{MAPbI}_3 \cdot \text{MACl} \cdot x\text{CH}_3\text{NH}_2$ is finally formed. The overall formation reaction of $\text{MAPbI}_3 \cdot \text{MACl} \cdot x\text{CH}_3\text{NH}_2$ is described as reaction 1, and the liquid state of the $\text{MAPbI}_3 \cdot \text{MACl} \cdot x\text{CH}_3\text{NH}_2$ precursor is confirmed in Figure S1 in the Supporting Information.

The $\text{MAPbI}_3 \cdot \text{MACl}$ solid contains two distinct phases, MAPbI_3 and MACl , as well as some other minor phases (MAPbCl_3 , PbI_2 , etc.) due to the facile solid-state ion-exchange in OIHPs, as determined using energy-dispersive spectroscopy (EDS), X-ray diffraction (XRD), and Raman spectroscopy (see Figures S2–S4). Therefore, to gain further insight into the $\text{MAPbI}_3 \cdot \text{MACl} - \text{CH}_3\text{NH}_2$ “fusing” process, the interactions of phase-pure MAPbI_3 and MACl solid particles with CH_3NH_2 gas were studied separately, and the results are presented in panels B and C of Figure 1, respectively. It is observed that both the MAPbI_3 and MACl solid particles also “melt” at the surface in the beginning and then transform to clear liquid drops with prolonged CH_3NH_2 -gas exposure at RT. It appears that the solid-to-liquid transformation occurs faster in the MACl case, which is consistent with the deliquescent nature of MACl .²⁴ This difference in the ingress kinetics of CH_3NH_2 into MAPbI_3 and MACl , as well as other coexisting phases, is responsible for the observed heterogeneous transformation behavior of the mixed-phase $\text{MAPbI}_3 \cdot \text{MACl}$ solid to the $\text{MAPbI}_3 \cdot \text{MACl} \cdot x\text{CH}_3\text{NH}_2$ liquid in Figure 1A.

Thin films of $\text{MAPbI}_3 \cdot \text{MACl} \cdot x\text{CH}_3\text{NH}_2$ liquid precursor were synthesized by exposing spin-coated $\text{MAPbI}_3 \cdot \text{MACl}$ thin films (random morphology) to CH_3NH_2 gas at RT. The as-synthesized $\text{MAPbI}_3 \cdot \text{MACl} \cdot x\text{CH}_3\text{NH}_2$ liquid-precursor thin films do not show any noticeable XRD peaks or absorption features in the visible-light region in panels B and C of Figure 2, respectively. While CH_3NH_2 in this liquid precursor can be released at RT when the CH_3NH_2 gas atmosphere is removed, the MACl component decomposes/sublimes only at an elevated temperature (e.g., 150°C). In this context, as illustrated schematically in Figure 2A, two steps are involved in the completion of the conversion of $\text{MAPbI}_3 \cdot \text{MACl} \cdot x\text{CH}_3\text{NH}_2$ precursor to phase-pure MAPbI_3 thin films. The

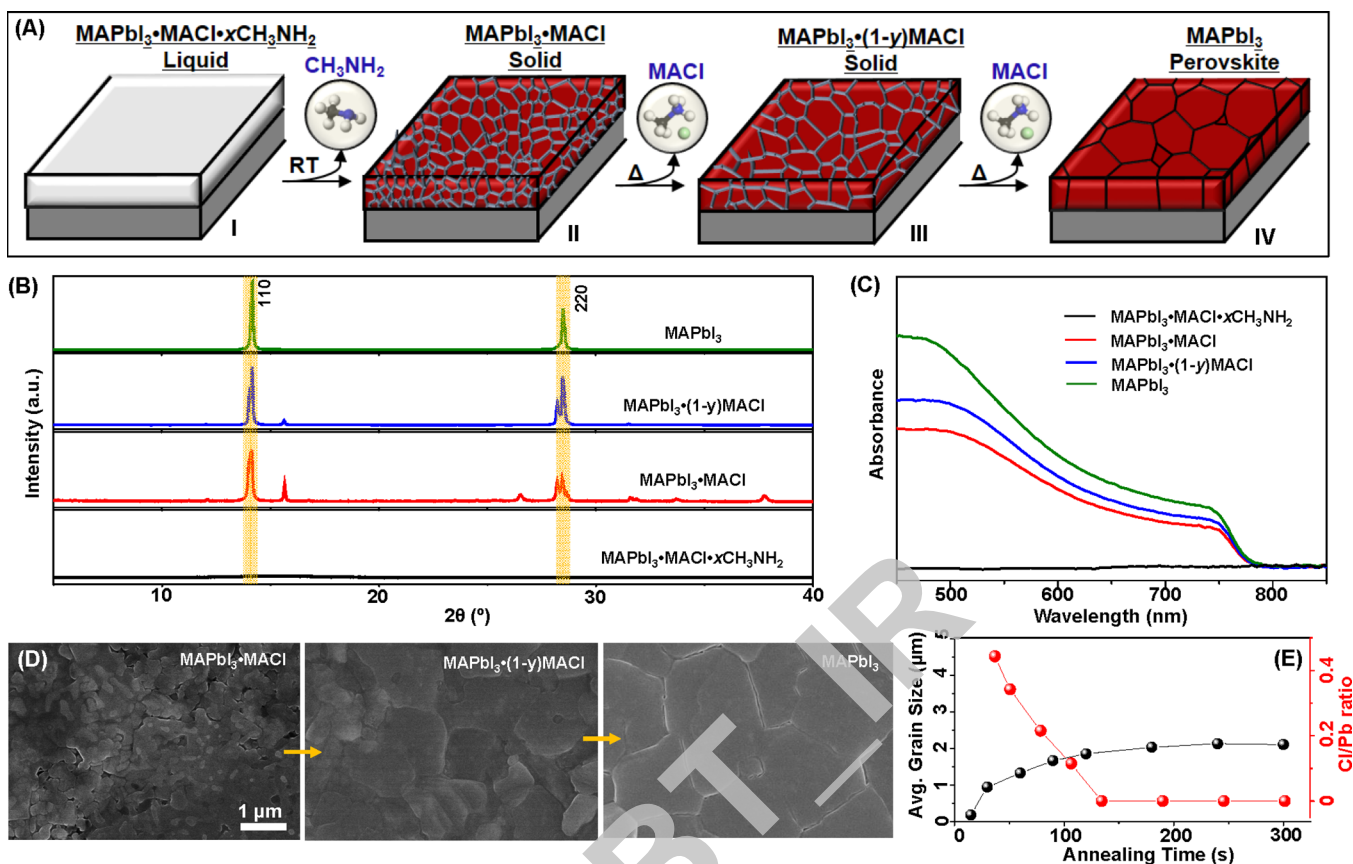
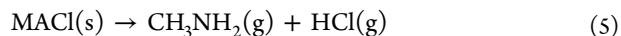
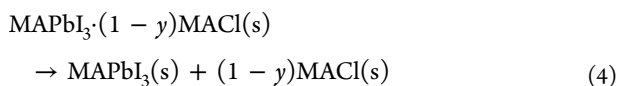
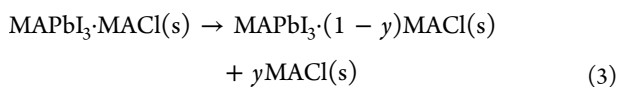
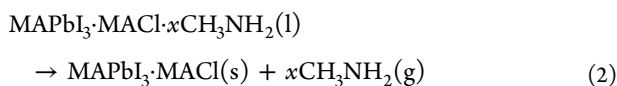
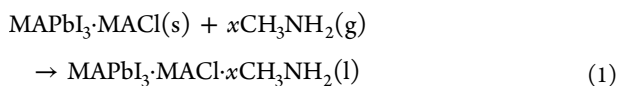


Figure 2. (A) Schematic illustration depicting the thin-film conversion process of MAPbI₃·MACl·xCH₃NH₂ liquid to MAPbI₃ OIHP. (B) XRD patterns and (C) UV-vis spectra of the thin film at different stages. Characteristic XRD peaks for MAPbI₃ are highlighted in panel B. (D) SEM images showing the surface morphologies of the thin film at different stages. (E) Plots of the average grain size and Cl/Pb atomic ratio in the thin film as a function of annealing time.

first step is the CH₃NH₂ self-degassing process at RT that results in the formation of MAPbI₃·MACl (reaction 2). The MAPbI₃·MACl thin film at this stage is expected to be textured and fine-grained, which is similar to what was reported earlier in the MAPbI₃·xCH₃NH₂ case.²⁰ In the next step, the MACl component in MAPbI₃·MACl gradually decomposes or releases upon annealing at 150 °C, forming MAPbI₃·(1 - y)MACl (y > 0) (reaction 3), and finally phase-pure MAPbI₃ OIHP forms (reaction 4), which is driven by MACl decomposition (reaction 5). Coupled with the chemical conversion, the small, uniaxially oriented MAPbI₃ grains coalesce and grow, forming a smooth compact MAPbI₃ OIHP thin film with large, uniaxially oriented grains and an ultralow-density GB-network.



The first step (reaction 2) in this new route is extremely facile. As seen in Figure 1A (images A3-A5), once the CH₃NH₂ gas atmosphere is removed, the MAPbI₃·MACl·xCH₃NH₂ precursor begins to convert to solid MAPbI₃·MACl, confirming that the release of CH₃NH₂ in MAPbI₃·MACl·xCH₃NH₂ occurs at RT without the need of any additional heating. This is consistent with the phase-pure MAPbI₃ and MACl cases shown in Figure 1B (images B3-B5) and Figure 1C (images C3-C5), respectively. In the case of nanoscale thin films, reaction 2 occurs in only a couple of seconds, as recorded in Figure S5. The as-formed MAPbI₃·MACl thin film retains the ultrasmooth morphology of the MAPbI₃·MACl·xCH₃NH₂ liquid and full-coverage, as confirmed in Figure 2D. For comparison, Figure S6 shows that MAPbI₃·MACl thin film deposited using the conventional one-step method has incomplete coverage. In Figure 2B, the XRD pattern of the as-formed MAPbI₃·MACl thin film indicates the presence of other phases, which is consistent with that of the MAPbI₃·MACl bulk sample (see Figure S3). A strong 110 texture is observed in the MAPbI₃ phase in Figure 2B, which implies that the as-crystallized MAPbI₃ grains in the thin film at this stage are preferentially oriented. The combination of the uniformity and the texture in the MAPbI₃·MACl thin film is the result of using the metastable MAPbI₃·MACl·xCH₃NH₂ precursor phase. This is key to the success in obtaining MAPbI₃ OIHP thin films with the target microstructures.

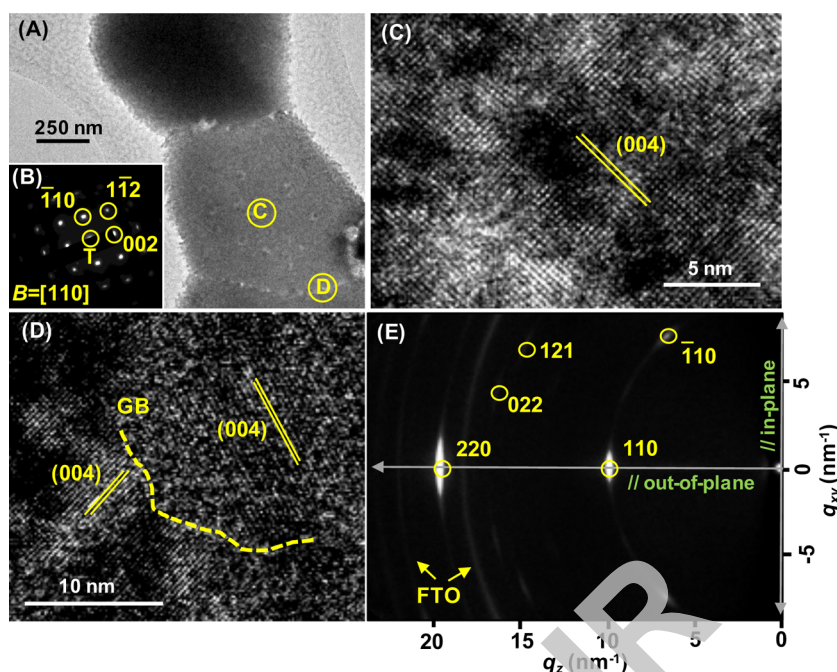


Figure 3. $\text{MAPbI}_3 \cdot \text{MACl} \cdot x\text{CH}_3\text{NH}_2$ -derived MAPbI_3 thin film: (A) bright-field TEM image, (B) indexed SAEDP (B = zone axis; T = transmitted beam), (C) HRTEM image of grain interior, (D) HRTEM image of GB, and (E) 2D XRD pattern.

For the next step, the thermal annealing drives the progression of reactions 3, 4, and 5. To elucidate the phase and microstructure evolution during this step, XRD patterns of the films annealed at 150 °C for different durations were collected, and the results are presented in Figure S7. It is found that a 120-s annealing duration is sufficient for achieving phase-pure MAPbI_3 OIHP thin films. A $\text{MAPbI}_3 \cdot (1-y)\text{MACl}$ thin film was also prepared by interrupting the annealing at 30 s. Figure 2B compares the XRD patterns of the $\text{MAPbI}_3 \cdot \text{MACl}$, the $\text{MAPbI}_3 \cdot (1-y)\text{MACl}$, and the final MAPbI_3 OIHP thin films. It is found that the intensity of the characteristic 110 XRD peak associated with MAPbI_3 OIHP increases, while the full width at half-maximum (fwhm) decreases with annealing duration (see Figure S8). This suggests that both the crystallinity and the size of the MAPbI_3 grains in the film have increased. Meanwhile, those XRD peaks that are associated with non- MAPbI_3 phases gradually disappear upon annealing, which reflects the progression of reactions 3, 4, and 5. Figure 2C shows ultraviolet–visible (UV–vis) spectra of the $\text{MAPbI}_3 \cdot \text{MACl}$, the $\text{MAPbI}_3 \cdot (1-y)\text{MACl}$, and the final MAPbI_3 OIHP thin films. The observed monotonic increase in the optical absorption upon annealing is in good agreement with the enhancement in the phase-purity, the crystallinity, and the grain size of the MAPbI_3 in the thin films.

Figure 2D compares surface morphologies of the $\text{MAPbI}_3 \cdot \text{MACl}$, the $\text{MAPbI}_3 \cdot (1-y)\text{MACl}$, and the final MAPbI_3 thin films as viewed by scanning electron microscopy (SEM). The $\text{MAPbI}_3 \cdot \text{MACl}$ thin film is composed of fine grains, but the GBs are not immediately distinguishable, which could be associated with the mixed-phase nature of $\text{MAPbI}_3 \cdot \text{MACl}$. The GBs, as well as GB grooves, in the $\text{MAPbI}_3 \cdot (1-y)\text{MACl}$ thin film become more clear, and the grain size increases up to $\sim 4 \mu\text{m}$ in the final MAPbI_3 OIHP thin film, which is an order-of-magnitude greater than the thickness of the thin film ($\sim 400 \text{ nm}$). Figure 2E plots the average grain size and the Cl:Pb atomic ratio in the film as a function of annealing time. The average grain sizes in these thin films were estimated using

image analyses of the SEM images (see Figure S9), and the atomic ratio Cl:Pb was monitored using EDS. It is clear that the increase in the average grain size is coupled with the decrease in the relative Cl content. The MAPbI_3 grain growth stagnates once Cl is fully depleted in the film. This indicates that the MACl -decomposition (reaction 5) is key to driving reactions 3 and 4 forward, as well as facilitating the coarsening of MAPbI_3 grains from an average grain size of 200 nm to 2.1 μm . In comparison, a reference- MAPbI_3 thin film made from the previously reported $\text{MAPbI}_3 \cdot x\text{CH}_3\text{NH}_2$ liquid precursor (MACl -free) shows a mean grain size of $\sim 280 \text{ nm}$, which is an order-of-magnitude smaller (see Figure S10). This highlights the exceptional role played by the MACl component in the metastable liquid precursor phase in determining the final microstructure of the MAPbI_3 OIHP thin films.

To confirm the characteristics of the grains and GB-network in the final MAPbI_3 OIHP thin films, transmission electron microscopy (TEM) characterization was performed. The TEM specimens were prepared by depositing thin films directly on holey-carbon-coated grids using the same procedure as above. Note that the grain size and coverage of the thin film on the TEM grid can be somewhat different because of the different wetting behavior of the $\text{MAPbI}_3 \cdot \text{MACl} \cdot x\text{CH}_3\text{NH}_2$ liquid on different substrates. However, this TEM specimen preparation method precludes unintended damage to MAPbI_3 grains during TEM specimen preparation using other methods such as focused ion beam (FIB), allowing us to unravel the real grain structure. The efficacy of this TEM specimen preparation method has been confirmed in previous studies by us and others.^{25,26} Figure 3A is a bright-field TEM image that shows micrometer-sized MAPbI_3 grains and associated GBs. The selected-area electron diffraction pattern (SAEDP; Figure 3B) and the high-resolution (HR) TEM image (Figure 3C) of the grain interior confirm the single-crystal nature of the MAPbI_3 grains in Figure 3A. Figure 3D shows the GB region, where the two grains show the same vertical orientation with 004 facets (β - MAPbI_3 , space group $I4/mcm$) exposed to the surface, i.e.,

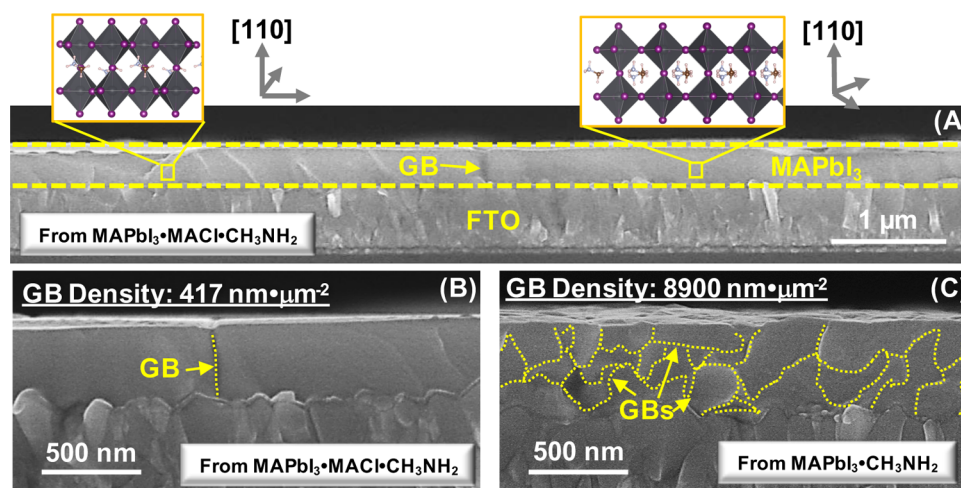


Figure 4. (A) Cross-sectional SEM image and schematic illustration of the grain orientations in the $\text{MAPbI}_3 \cdot \text{MACl} \cdot x\text{CH}_3\text{NH}_2$ -derived MAPbI_3 thin film. Higher-magnification cross-sectional SEM images and comparison of the GB-network density: (B) $\text{MAPbI}_3 \cdot \text{MACl} \cdot x\text{CH}_3\text{NH}_2$ -derived MAPbI_3 thin film and (C) reference MAPbI_3 thin film. GB-density is defined as the total GB length divided by the relevant cross-sectional area.

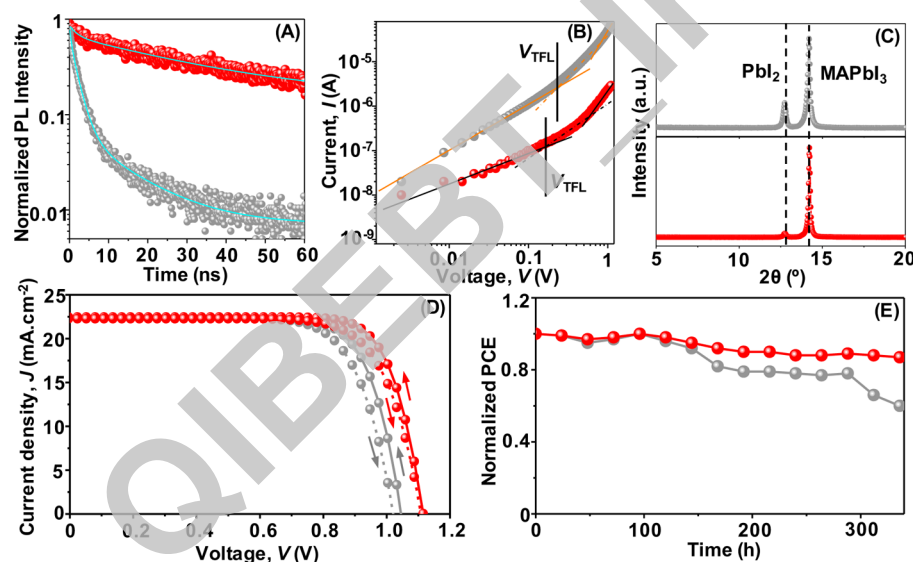


Figure 5. $\text{MAPbI}_3 \cdot \text{MACl} \cdot x\text{CH}_3\text{NH}_2$ -derived MAPbI_3 (red) and reference MAPbI_3 (gray) thin films: (A) time-resolved PL decay, (B) dark I – V response in a capacitor-like device, (C) XRD patterns after 24 h of storage in the ambient, (D) J – V curves of PSCs made using the respective thin films, and (E) PCE evolution of the respective PSCs as a function of storage time in the ambient. The extracted property–performance parameters are summarized in Table 1.

110-oriented. For comparison, the reference MAPbI_3 OIHP thin film that is also directly deposited on the TEM grid from the $\text{MAPbI}_3 \cdot x\text{CH}_3\text{NH}_2$ precursor liquid (MACl-free) has a much smaller grain size and shows multiple layers of grains (see Figure S11). Figure 3E presents a two-dimensional (2D) XRD pattern of the $\text{MAPbI}_3 \cdot \text{MACl} \cdot x\text{CH}_3\text{NH}_2$ -derived MAPbI_3 thin film. Intense diffraction spots (indexed) with negligible spread along the Debye–Scherrer ring are observed, further confirming the strong uniaxial 110-orientation of the MAPbI_3 grains.

These characterization results confirm that the $\text{MAPbI}_3 \cdot \text{MACl} \cdot x\text{CH}_3\text{NH}_2$ -derived MAPbI_3 thin film comprises ultra-large grains spanning the film thickness that have the same vertical 110-orientation but different horizontal orientations (“mosaic” texture). Only vertical GBs are present in the film, which is illustrated schematically in Figure 4A. The density of the GB-network in the film cross section is estimated at only

$\sim 417 \text{ nm} \cdot \mu\text{m}^{-2}$ (Figure 4B). For comparison, Figure 4C shows the cross section of the reference MAPbI_3 thin film, where random GB-network with significantly higher density (~ 20 times) is observed.

The simultaneous evolution of large, uniaxially oriented grains and an ultralow-density GB-network is found to have profound effect in enhancing the optoelectronic properties of the MAPbI_3 OIHP thin films, as well as their environmental stability. Figure 5A compares the time-resolved photoluminescence (PL) decay of the $\text{MAPbI}_3 \cdot \text{MACl} \cdot x\text{CH}_3\text{NH}_2$ -derived MAPbI_3 and the reference MAPbI_3 thin films. The amplitude-weighted average lifetime (τ) is estimated at 24.2 ns for the $\text{MAPbI}_3 \cdot \text{MACl} \cdot x\text{CH}_3\text{NH}_2$ -derived MAPbI_3 thin film, which is much longer than that for the reference MAPbI_3 thin film (3.8 ns). The defect density (N) in both films is also estimated by monitoring the evolution of the space-charge-limited currents (in the dark) as a function of the bias voltage in

Table 1. Summary of the Property–Performance Parameters Extracted from the Data in Figure 5^a

	τ (ns)	V_{TFL} (V)	D (%)		J_{SC} (mA cm ⁻²)	V_{OC} (V)	FF	PCE (%)	avg. PCE (%)	R (%)
I	24.2	0.169	5	forward	22.5	1.12	0.770	19.4	18.9	87
				reverse	22.3	1.11	0.733	18.1		
II	3.8	0.219	28	forward	22.4	1.04	0.758	17.6	17.1	60
				reverse	22.4	1.02	0.728	16.6		

^aI and II indicate MAPbI₃·MAcI·xCH₃NH₂-derived MAPbI₃ and reference MAPbI₃ thin films, respectively. τ is the amplitude-weighted average lifetime based on biexponential fitting of the time-resolved PL decay. V_{TFL} is the trap-filling limited voltage. D is the ratio of the XRD peak intensities of PbI₂ to MAPbI₃ in Figure 5C. J_{SC} , V_{OC} , FF, and PCE are short-circuit density, open-circuit voltage, fill factor, and power conversion efficiency of the PSC, respectively. Reported avg PCEs are the average of the PCE values for forward and reverse scans. R is the retention of PCE after the PSC is stored for 336 h in the ambient.

capacitor-like devices (see the Supporting Information for details). As shown in Figure 5B, the trap-filling limited voltage (V_{TFL}) is determined by the kink point where the current increase becomes nonlinear.²⁷ The relationship between V_{TFL} and N is given by the equation, $V_{\text{TFL}} = \frac{eNL^2}{2\epsilon\epsilon_0}$, where e is the elementary charge, L the film thickness, ϵ relative dielectric constant, and ϵ_0 the vacuum permittivity.²⁷ The values of N in the MAPbI₃·MAcI·xCH₃NH₂-derived MAPbI₃ and the reference-MAPbI₃ thin film are calculated to be 8.85×10^{15} cm⁻³ and 1.15×10^{16} cm⁻³, respectively. The reduced N in the MAPbI₃·MAcI·xCH₃NH₂-derived MAPbI₃ thin film is in good agreement with the prolonged PL lifetime. The ambient stability of both films was also evaluated. Figure 5C shows XRD patterns from both films after 24 h of storage in the ambient. Negligible decomposition to PbI₂ is observed in the MAPbI₃·MAcI·xCH₃NH₂-derived MAPbI₃ thin film, whereas a large amount of PbI₂ is found in the reference MAPbI₃ thin film. It is recognized that the main cause of the MAPbI₃ thin film degradation in the ambient is the ingress of moisture into the MAPbI₃ crystalline structure, where Wang et al.¹² have recently shown that the GB regions in MAPbI₃ films allow fast ingress of moisture.

In this context, additional experiments were performed to study the beneficial role of ultralow-density GB-network in the MAPbI₃·MAcI·xCH₃NH₂-derived MAPbI₃ film on their moisture tolerance. Because the MAPbI₃ OIHP thin film is sandwiched between a TiO₂ electron-transporting layer (ETL) and a Spiro-OMeTAD hole-transporting layer (HTL) in a typical PSC, the following experiment was designed to simulate to some extent the MAPbI₃ degradation behavior in a real PSC. As shown in Figure S12A,B, identical Spiro-OMeTAD HTL layers were drop-coated on the centers of the MAPbI₃·MAcI·xCH₃NH₂-derived MAPbI₃ and the reference-MAPbI₃ thin films (on TiO₂-coated FTO substrates). The film structures were then stored in the ambient for 96 h, and the Spiro-OMeTAD layers were then washed away. Figure S12C,D shows the morphologies of the MAPbI₃ thin films at different locations in the previously Spiro-OMeTAD-covered region for both samples. It is clear that the moisture-induced degradation propagates from the Spiro-OMeTAD edge to the center along the GB network. In this context, the highly reduced GB density in the MAPbI₃·MAcI·xCH₃NH₂-derived MAPbI₃ thin film effectively slows down the degradation kinetics, as illustrated in Figure S12E.

PSCs were fabricated to evaluate the performance of the MAPbI₃·MAcI·xCH₃NH₂-derived MAPbI₃ film. PSCs based on the reference MAPbI₃ thin film were also fabricated for comparison. Figure 5D shows the current density–voltage (J – V) curves from the PSCs that exhibit very small J – V hysteresis.

The overall PCE for the PSC made using the MAPbI₃·MAcI·xCH₃NH₂-derived MAPbI₃ thin film is 19.4% (reverse scan), which is higher than that (17.6%) for the PSC using the reference MAPbI₃ thin film. A more detailed comparison in PCE values for both PSCs is shown in Table 1. Figure S13 shows PCE statistics of the PSCs made using the MAPbI₃·MAcI·xCH₃NH₂-derived MAPbI₃ thin films, which attests to the excellent reproducibility of the thin-film processing method described here. It can be seen from the performance parameters of both PSCs in Table 1 that the PCE increase for the MAPbI₃·MAcI·xCH₃NH₂-derived MAPbI₃ thin film can be attributed mostly to the enhancement of the V_{OC} . This is consistent with the reduced nonradiative recombination²⁸ due to lower defect density in the MAPbI₃·MAcI·xCH₃NH₂-derived MAPbI₃ thin film, as revealed in Figure 5A,B. Finally, the PCE evolution as a function of storage time in the ambient for both PSCs are shown in Figure 5E. Compared with the 60% retention in the PSC using the reference MAPbI₃ film, the PSC made using the MAPbI₃·MAcI·xCH₃NH₂-derived MAPbI₃ thin film retains 87% of its initial PCE after 336 h of storage in the ambient. This is closely related to the inherently higher moisture tolerance observed in the MAPbI₃·MAcI·xCH₃NH₂-derived MAPbI₃ thin film in Figures S12 and 5C. Once again, all these enhanced performance parameters in the PSC using the MAPbI₃·MAcI·xCH₃NH₂-derived MAPbI₃ thin film highlight the benefits of their unique thin-film microstructures.

In closing, we have demonstrated the use of a new liquid precursor, MAPbI₃·MAcI·xCH₃NH₂, with engineered metastability, for the processing of MAPbI₃ OIHP thin films. The resulting MAPbI₃ thin film exhibit a unique combination of microstructural features: large, uniaxially oriented (“mosaic” texture) grains spanning the film thickness and ultralow-density GB-network with only vertical GBs. This near-ideal microstructure of the MAPbI₃ OIHP thin film contributes to their superior optoelectronic and environmental-stability properties and results in the enhanced performance of the PSCs made using these thin films. This study points to a new direction in the tailoring of the chemistry and the metastability of the precursor phase for achieving targeted microstructures in OIHP thin films and more efficient and durable PSCs.

■ ASSOCIATED CONTENT

§ Supporting Information

The Supporting Information is available free of charge on the ACS Publications website at DOI: 10.1021/acsenergylett.7b00980.

Experimental section and additional characterization and analysis data for the precursor phases, OIHP films, and PSCs (PDF)

AUTHOR INFORMATION

Corresponding Authors

*E-mail: pangsp@qibebt.ac.cn.

*E-mail: nitin_padtire@brown.edu.

*E-mail: yuanyuan_zhou@brown.edu.

ORCID

Shuping Pang: 0000-0002-2526-4104

Guanglei Cui: 0000-0002-8008-7673

Nitin P. Padture: 0000-0001-6622-8559

Notes

The authors declare no competing financial interest.

ACKNOWLEDGMENTS

S.P., F.J., and G.C. thank the National Natural Science Foundation of China (51672290, 21671196) and the Youth Innovation Promotion Association of CAS (2015167). Y. Zhou, L.Z., Y. Zong and N.P.P. acknowledge the research funding from the Office of Naval Research (N00014-17-1-2232) and the National Science Foundation (OIA-1538893).

REFERENCES

- (1) Stranks, S. D.; Snaith, H. J. Metal-halide Perovskites for Photovoltaic and Light-Emitting Devices. *Nat. Nanotechnol.* **2015**, *10*, 391–402.
- (2) Kim, H.-S.; Lee, C.-R.; Im, J.-H.; Lee, K.-B.; Moehl, T.; Marchioro, A.; Moon, S.-J.; Humphry-Baker, R.; Yum, J.-H.; Moser, J. E.; et al. Lead Iodide Perovskite Sensitized All-Solid-State Submicron Thin Film Mesoscopic Solar Cell with Efficiency Exceeding 9%. *Sci. Rep.* **2012**, *2*, 591.
- (3) Kojima, A.; Teshima, K.; Shirai, Y.; Miyasaka, T. Organometal Halide Perovskites as Visible-Light Sensitizers for Photovoltaic Cells. *J. Am. Chem. Soc.* **2009**, *131*, 6050–6051.
- (4) Yang, W. S.; Park, B.-W.; Jung, E. H.; Jeon, N. J.; Kim, Y. C.; Lee, D. U.; Shin, S. S.; Seo, J.; Kim, E. K.; Noh, J. H.; et al. Iodide Management in Formamidinium-Lead-Halide-Based Perovskite Layers for Efficient Solar Cells. *Science* **2017**, *356*, 1376–1379.
- (5) Zhou, Y.; Zhu, K. Perovskite Solar Cells Shine in the “Valley of the Sun”. *ACS Energy Letters* **2016**, *1*, 64–67.
- (6) Huang, J.; Shao, Y.; Dong, Q. Organometal Trihalide Perovskite Single Crystals: A Next Wave of Materials for 25% Efficiency Photovoltaics and Applications Beyond? *J. Phys. Chem. Lett.* **2015**, *6*, 3218–3227.
- (7) Zhou, Y.; Game, O. S.; Pang, S.; Padture, N. P. Microstructures of Organometal Trihalide Perovskites for Solar Cells: Their Evolution from Solutions and Characterization. *J. Phys. Chem. Lett.* **2015**, *6*, 4827–4839.
- (8) Docampo, P.; Hanusch, F. C.; Giesbrecht, N.; Angloher, P.; Ivanova, A.; Bein, T. Influence of the Orientation of Methylammonium Lead Iodide Perovskite Crystals on Solar Cell Performance. *APL Mater.* **2014**, *2*, 081508.
- (9) Kim, D. H.; Park, J.; Li, Z.; Yang, M.; Park, J. S.; Park, I. J.; Kim, J. Y.; Berry, J. J.; Rumbles, G.; Zhu, K. 300% Enhancement of Carrier Mobility in Uniaxial-Oriented Perovskite Films Formed by Topotactic-Oriented Attachment. *Adv. Mater.* **2017**, *29*, 1606831.
- (10) Guo, Y.; Sato, W.; Shoyama, K.; Halim, H.; Itabashi, Y.; Shang, R.; Nakamura, E. Citric Acid Modulated Growth of Oriented Lead Perovskite Crystals for Efficient Solar Cells. *J. Am. Chem. Soc.* **2017**, *139*, 9598–9604.
- (11) Wang, Y.; Shi, Y.; Xin, G.; Lian, J.; Shi, J. Two Dimensional van der Waals Epitaxy Kinetics in a Three-Dimensional Perovskite Halide. *Cryst. Growth Des.* **2015**, *15*, 4741–4749.
- (12) Wang, Q.; Chen, B.; Liu, Y.; Deng, Y.; Bai, Y.; Dong, Q.; Huang, J. Scaling Behavior of Moisture-Induced Grain Degradation in Polycrystalline Hybrid Perovskite Thin Films. *Energy Environ. Sci.* **2017**, *10*, 516–522.
- (13) Yin, W. J.; Shi, T.; Yan, Y. Unique Properties of Halide Perovskites as Possible Origins of the Superior Solar Cell Performance. *Adv. Mater.* **2014**, *26*, 4653–4658.
- (14) Jeon, N. J.; Noh, J. H.; Kim, Y. C.; Yang, W. S.; Ryu, S.; Seok, S. I. Solvent Engineering for High-Performance Inorganic–Organic Hybrid Perovskite Solar Cells. *Nat. Mater.* **2014**, *13*, 897–903.
- (15) Xiao, Z.; Dong, Q.; Bi, C.; Shao, Y.; Yuan, Y.; Huang, J. Solvent Annealing of Perovskite-Induced Crystal Growth for Photovoltaic-Device Efficiency Enhancement. *Adv. Mater.* **2014**, *26*, 6503–6509.
- (16) Huang, F.; Dkhissi, Y.; Huang, W.; Xiao, M.; Benesperi, I.; Rubanov, S.; Zhu, Y.; Lin, X.; Jiang, L.; Zhou, Y.; et al. Gas-Assisted Preparation of Lead Iodide Perovskite Films Consisting of a Monolayer of Single Crystalline Grains for High Efficiency Planar Solar Cells. *Nano Energy* **2014**, *10*, 10–18.
- (17) Zhou, Y.; Yang, M.; Wu, W.; Vasiliev, A. L.; Zhu, K.; Padture, N. P. Room-Temperature Crystallization of Hybrid-Perovskite Thin Films via Solvent-solvent Extraction for High-Performance Solar Cells. *J. Mater. Chem. A* **2015**, *3*, 8178–8184.
- (18) Zhao, Y.; Zhu, K. CH₃NH₃Cl-Assisted One-Step Solution Growth of CH₃NH₃PbI₃: Structure, Charge-Carrier Dynamics, and Photovoltaic Properties of Perovskite Solar Cells. *J. Phys. Chem. C* **2014**, *118*, 9412–9418.
- (19) Chen, A. Z.; Foley, B. J.; Ma, J. H.; Alpert, M. R.; Niezgoda, J. S.; Choi, J. J. Crystallographic Orientation Propagation in Metal Halide Perovskite Thin Films. *J. Mater. Chem. A* **2017**, *5*, 7796–7800.
- (20) Zhou, Z.; Wang, Z.; Zhou, Y.; Pang, S.; Wang, D.; Xu, H.; Liu, Z.; Padture, N. P.; Cui, G. Methylamine-Gas-Induced Defect-Healing Behavior of CH₃NH₃PbI₃ Thin Films for Perovskite Solar Cells. *Angew. Chem., Int. Ed.* **2015**, *54*, 9705–9709.
- (21) Zhou, Y.; Padture, N. P. Gas-Induced Formation/Transformation of Organic-Inorganic Halide Perovskites. *ACS Energy Letters* **2017**, *2*, 2166–2176.
- (22) Pang, S.; Zhou, Y.; Wang, Z.; Yang, M.; Krause, A. R.; Zhou, Z.; Zhu, K.; Padture, N. P.; Cui, G. Transformative Evolution of Organolead Triiodide Perovskite Thin Films from Strong Room-Temperature Solid–Gas Interaction Between HPbI₃–CH₃NH₂ Precursor Pair. *J. Am. Chem. Soc.* **2016**, *138*, 750–753.
- (23) Yu, H.; Wang, F.; Xie, F.; Li, W.; Chen, J.; Zhao, N. The Role of Chlorine in the Formation Process of “CH₃NH₃PbI_{3-x}Cl_x” Perovskite. *Adv. Funct. Mater.* **2014**, *24*, 7102–7108.
- (24) Hughes, E. W.; Lipscomb, W. N. The Crystal Structure of Methylammonium Chloride. *J. Am. Chem. Soc.* **1946**, *68*, 1970–1975.
- (25) Rothmann, M. U.; Li, W.; Zhu, Y.; Bach, U.; Spiccia, L.; Etheridge, J.; Cheng, Y.-B. Direct Observation of Intrinsic Twin Domains in Tetragonal CH₃NH₃PbI₃. *Nat. Commun.* **2017**, *8*, 14547.
- (26) Zhou, Y.; Vasiliev, A. L.; Wu, W.; Yang, M.; Pang, S.; Zhu, K.; Padture, N. P. Crystal Morphologies of Organolead Trihalide in Mesoscopic/Planar Perovskite Solar Cells. *J. Phys. Chem. Lett.* **2015**, *6*, 2292–2297.
- (27) Liu, Z.; Hu, J.; Jiao, H.; Li, L.; Zheng, G.; Chen, Y.; Huang, Y.; Zhang, Q.; Shen, C.; Chen, Q.; et al. Chemical Reduction of Intrinsic Defects in Thicker Heterojunction Planar Perovskite Solar Cells. *Adv. Mater.* **2017**, *29*, 1606774.
- (28) Huang, J.; Yuan, Y.; Shao, Y.; Yan, Y. Understanding the Physical Properties of Hybrid Perovskites for Photovoltaic Applications. *Nat. Rev. Mater.* **2017**, *2*, 17042.

Supporting Information

Simultaneous Evolution of Uniaxially-Oriented Grains and Ultralow-Density Grain-Boundary Network in $\text{CH}_3\text{NH}_3\text{PbI}_3$ Perovskite Films Mediated by Precursor-Phase Metastability

Fuxiang Ji,[†] Shuping Pang,[†] Lin Zhang,[‡] Yingxia Zong,[‡] Guanglei Cui,[†] Nitin P. Padture^{‡,*} and Yuanyuan Zhou^{‡,*}

[†] Qingdao Institute of Bioenergy and Bioprocess Technology, Chinese Academy of Sciences, 189 Songling Road, Qingdao 266101, P.R. China *Email: pangsp@qibebt.ac.cn

[‡] School of Engineering, Brown University, 184 Hope Street, Providence, Rhode Island 02912, United States *Email: nitin_padture@brown.edu; yuanyuan_zhou@brown.edu

Experimental Section

Materials Synthesis and Films Fabrication. All the raw chemicals were obtained commercially without further purification. Typically, the methylamine (CH_3NH_2) gas was generated using commercially purchased CH_3NH_2 gas (Sigma-Aldrich, USA) tank or a CH_3NH_2 ethanol solution (27-32 wt%, Sinopharm, China). For typical synthesis of the $\text{MAPbI}_3 \cdot \text{MACl}$ powder and thin film samples, MAI (Dyesol, Australia), PbI_2 (Alfa Aesar, USA), and MACl (Sigma-Aldrich, USA) in molar ratio of 1:1:1 were co-dissolved in dimethylformamide (DMF, Sigma-Aldrich, USA) to form a 40 wt% solution. The $\text{MAPbI}_3 \cdot \text{MACl}$ powders were prepared by drop-casting the solution onto substrates and evaporating away the DMF at 100 °C. The $\text{MAPbI}_3 \cdot \text{MACl}$ thin films were fabricated by spin-coating the solution on substrates at 4500 rpm for 40 s, followed by thermal annealing at 100 °C for 3 min. In order to form the $\text{MAPbI}_3 \cdot \text{MACl} \cdot \text{CH}_3\text{NH}_2$ liquid film, the $\text{MAPbI}_3 \cdot \text{MACl}$ films were exposed to the CH_3NH_2 gas until the solids were completely liquefied and bleached. The $\text{MAPbI}_3 \cdot \text{MACl} \cdot \text{CH}_3\text{NH}_2$ liquid film was then removed from the CH_3NH_2 gas with the formation of smooth dark-brown solid thin film, which was subsequently annealed at 150 °C for different periods of time on a hotplate. The phase-purity and microstructures of the final MAPbI_3 films are dependent of the annealing duration. Optimal MAPbI_3 thin films are prepared by annealing at 150 °C for 120 s. Reference- MAPbI_3 thin films were deposited without addition of MACl.

Materials and Film Characterization. X-ray diffraction (XRD) patterns were obtained using an X-ray diffractometer (D8 Advance, Bruker, Germany) using Cu K_α radiation, with 0.02° step size. The 2D XRD maps were collected using the same diffractometer equipped with a 2D detector (Vantec 500, Germany). UV-vis absorption spectra of the films were recorded using a spectrometer (U-4100, Hitachi, Japan). UV-vis measurements on the films under CH_3NH_2 gas were performed on samples sealed between quartz windows. A field-emission scanning electron microscope (SEM; S-4800, Hitachi, Japan) was used to observe the top surfaces and the cross-sections. High-resolution characterization was performed using a transmission electron microscope (TEM; 2100F, JEOL, Japan) operated at 200 kV accelerating voltage. Thin films for TEM studies were prepared using the same procedure as above, but were deposited directly on TEM grids (SPI, USA). Raman spectroscopy was performed on a Raman microscope (DXR™2, Thermo Fisher Scientific, USA) with a 532-nm laser excitation. *In situ* optical microscopy observations were carried out using a stereomicroscope (SZX16, Olympus, Japan). These experiments were conducted by placing the $\text{MAPbI}_3 \cdot \text{MACl}$, MAPbI_3 and MACl samples in a home-made gas chamber with transparent windows (transmittance >95%). A gas nozzle was used to introduce CH_3NH_2 atmosphere around the sample. Time-resolved photoluminescence (PL) measurements were performed on a commercial spectrophotometer (FLS980, Edinburgh Instruments, UK) with a 441-nm laser excitation. In order to estimate the trap density (N) in the MAPbI_3 film, the current-voltage (I - V) scan of the device with the MAPbI_3 film sandwiched by two n-type contacts (FTO/ TiO_2 and PCBM/Au) is performed on a 2400 sourcemeter (Keithley, USA) in

dark. The trap-filled limited voltage (V_{TFL}) is then determined by the kink point where the current increase becomes non-linear in the I - V curve. The relationship of V_{TFL} with N is defined by the equation $V_{\text{TFL}} = \frac{eNL^2}{2\epsilon\epsilon_0}$, where e is the elementary charge, L is the film thickness, ϵ is relative dielectric constant, and ϵ_0 is the vacuum permittivity.^[S1]

Solar Cell Fabrication and Testing. To fabricate perovskite solar cells (PSCs), a 30-nm compact-TiO₂ layer was solution-deposited on top of the pre-patterned FTO-glass substrate using a reported procedure.^[S2] A 250-nm mesoporous-TiO₂ layer was then deposited by spin-coating a dilute commercial TiO₂ paste at 4000 rpm, 45 s, followed by sintering at 550 °C for 30 min in air. The MAPbI₃ perovskite layer were then deposited using the procedures described above. A solution of Spiro-MeOTAD (99%) hole-transporting layer (HTL) coating was prepared by dissolving 72.3 mg of Spiro-MeOTAD in 1 mL of chlorobenzene (99.8%), to which 28.8 μ L of 4-tert-butyl pyridine and 17.5 μ L of lithium bis(trifluoromethanesulfonyl)imide (LITSFI) solution (520 mg LITSFI (98%) in 1 mL acetonitrile (99.8%)) were added. The HTL was deposited by spin-coating (3000 rpm, 30 s). Finally, a 100-nm Ag electrode was thermally-evaporated to complete the solar cells. The HTL and the Ag layers were then deposited to complete the PSC assembly. Current density-voltage (J - V) characteristics of the as-fabricated PSCs were measured using a 2400 Sourcemeeter (Keithley, USA) under simulated one-sun AM 1.5G 100 mW.cm⁻² intensity (Oriel Sol3A Class AAA, Newport, USA), under both reverse (from open circuit voltage, V_{OC} , to short-circuit current density, J_{SC}) and forward (from J_{SC} to V_{OC}) scans. The step voltage was 50 mV with a 10 ms delay time per step. The J - V output was converted to PCE output using the following relation: $\text{PCE} = \{J (\text{mA.cm}^{-2}) \times V (\text{V})\} / (100 (\text{mW.cm}^{-2}))$. The external quantum efficiency (EQE) spectra were recorded with an EQE measurement system (PVE 300, Bentham, UK) comprised of a Xenon lamp, a monochromator, a chopper, a lock-in amplifier, and a calibrated silicon photodetector. A shutter was used to switch on and off the one-sun illumination on the PSC. Typical active area of the PSCs is 0.09 cm² defined using a non-reflective metal mask. The intensity of the one-sun AM 1.5G (100 mW.cm²) illumination was calibrated using a Si-reference cell certified by the National Renewable Energy Laboratory.

References

- [S1] Z. Liu, J. Hu, H. Jiao, L. Li, G. Zheng, Y. Chen, Y. Huang, Q. Zhang, C. Shen, Q. Chen, H. Zhou, *Adv. Mater.*, 2017, 29, 1606774.
 [S2] S. Lv, S. Pang, Y. Zhou, N. P. Padture, H. Hu, L. Wang, X. Zhou, H. Zhu, L. Zhang, C. Huang, G. Cui, *Phys. Chem. Chem. Phys.*, 2014, 16, 19206-19211.

Supplementary Figures



Figure S1. Photograph of MAPbI₃•MACl•xCH₃NH₂ precursor under CH₃NH₂ gas in an inclined sample bottle showing its liquid nature.

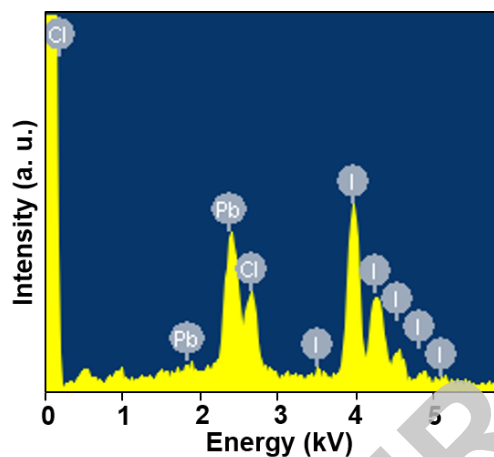


Figure S2. EDS spectrum of the MAPbI₃•MACl sample showing the presence of Cl.

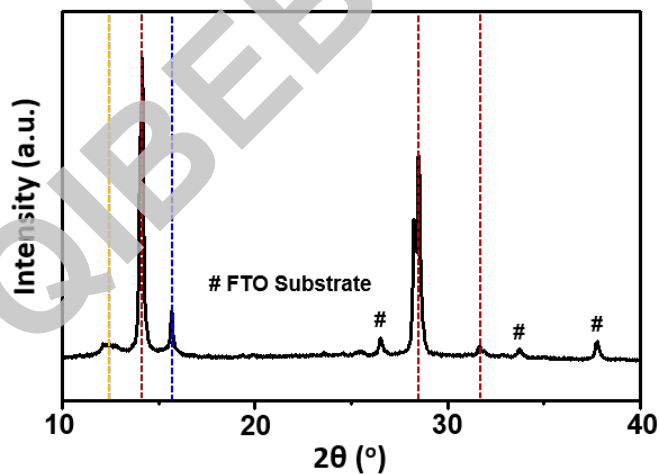


Figure S3. XRD pattern of the MAPbI₃•MACl sample showing multiple phases. The peaks labeled by yellow, red, and blue dashed lines are assigned to PbI₂, MAPbI₃, and MAPbCl₃, respectively. Other amorphous and low-crystallinity phases such as MACl, which do not show XRD signal, may also exist in the sample.

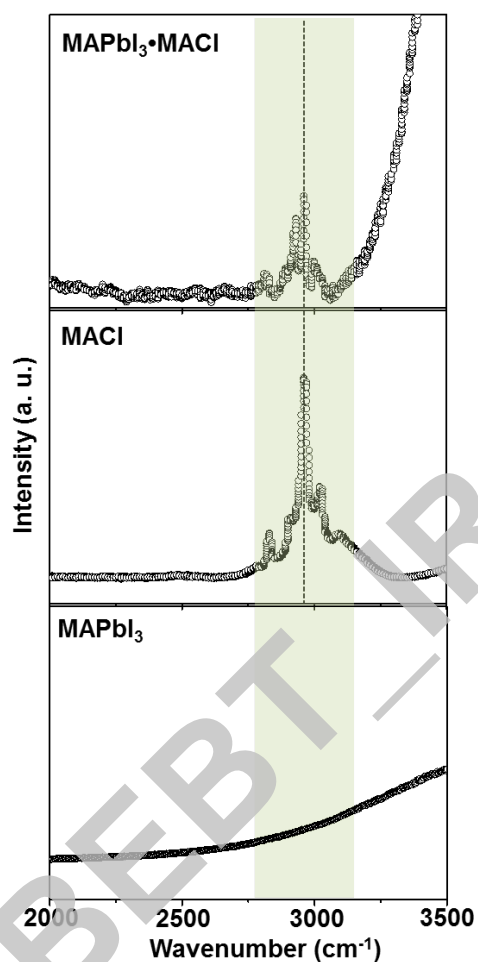


Figure S4. Raman spectra of the $\text{MAPbI}_3 \cdot \text{MACl}$, MACl , and MAPbI_3 samples showing the same characteristic bands in $\text{MAPbI}_3 \cdot \text{MACl}$ and MACl , but no bands in MAPbI_3 in the highlighted wavenumber range.

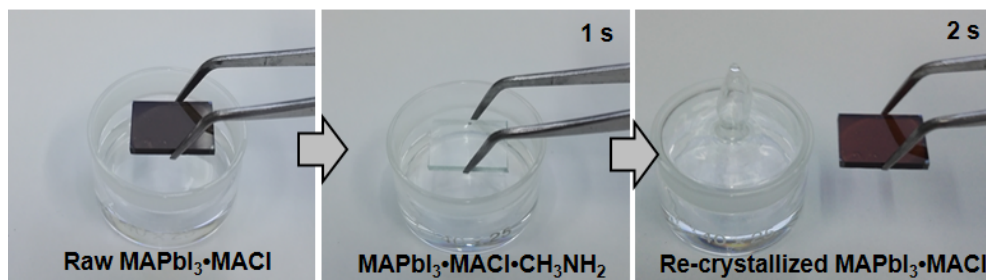


Figure S5. Photographs showing a nominal, initial $\text{MAPbI}_3 \cdot \text{MACl}$ thin film (left), the formation of an $\text{MAPbI}_3 \cdot \text{MACl} \cdot x\text{CH}_3\text{NH}_2$ liquid thin film upon exposure to the CH_3NH_2 gas at RT (middle), and RT-recrystallization of a smooth $\text{MAPbI}_3 \cdot \text{MACl}$ thin film after removal of the CH_3NH_2 gas at RT (right).

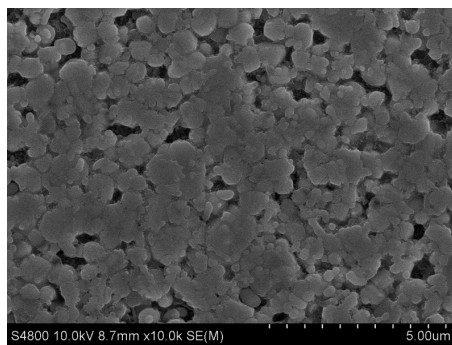


Figure S6. SEM micrograph of top surface of the initial MAPbI₃•MACl film.

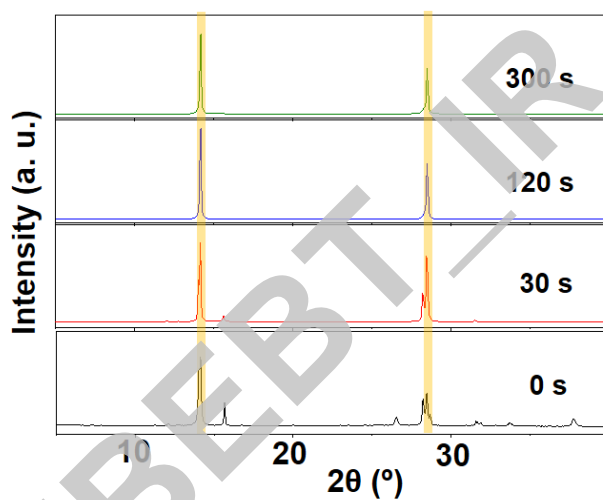


Figure S7. XRD patterns of the recrystallized smooth MAPbI₃•MACl thin film after annealing at 150 °C for different durations. Characteristic XRD peaks for MAPbI₃ are highlighted.

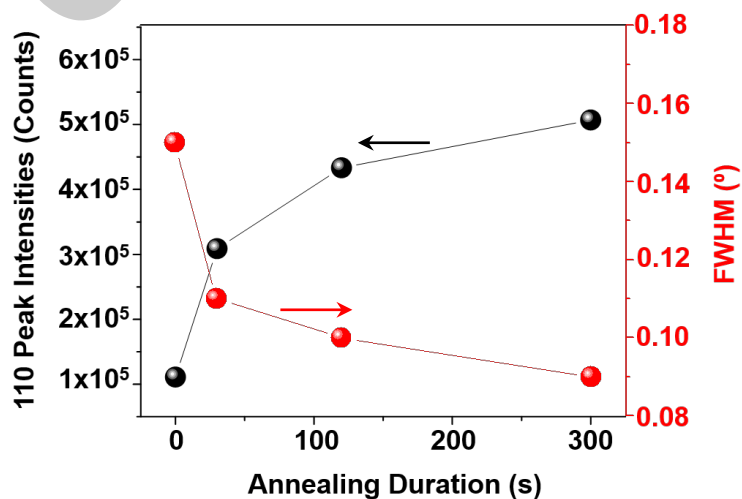


Figure S8. Variation of the intensity and full-width-at-half-maximum (FWHM) of the characteristic 110 XRD peaks of MAPbI₃ in the RT-recrystallized MAPbI₃•MACl film after annealing for different durations.

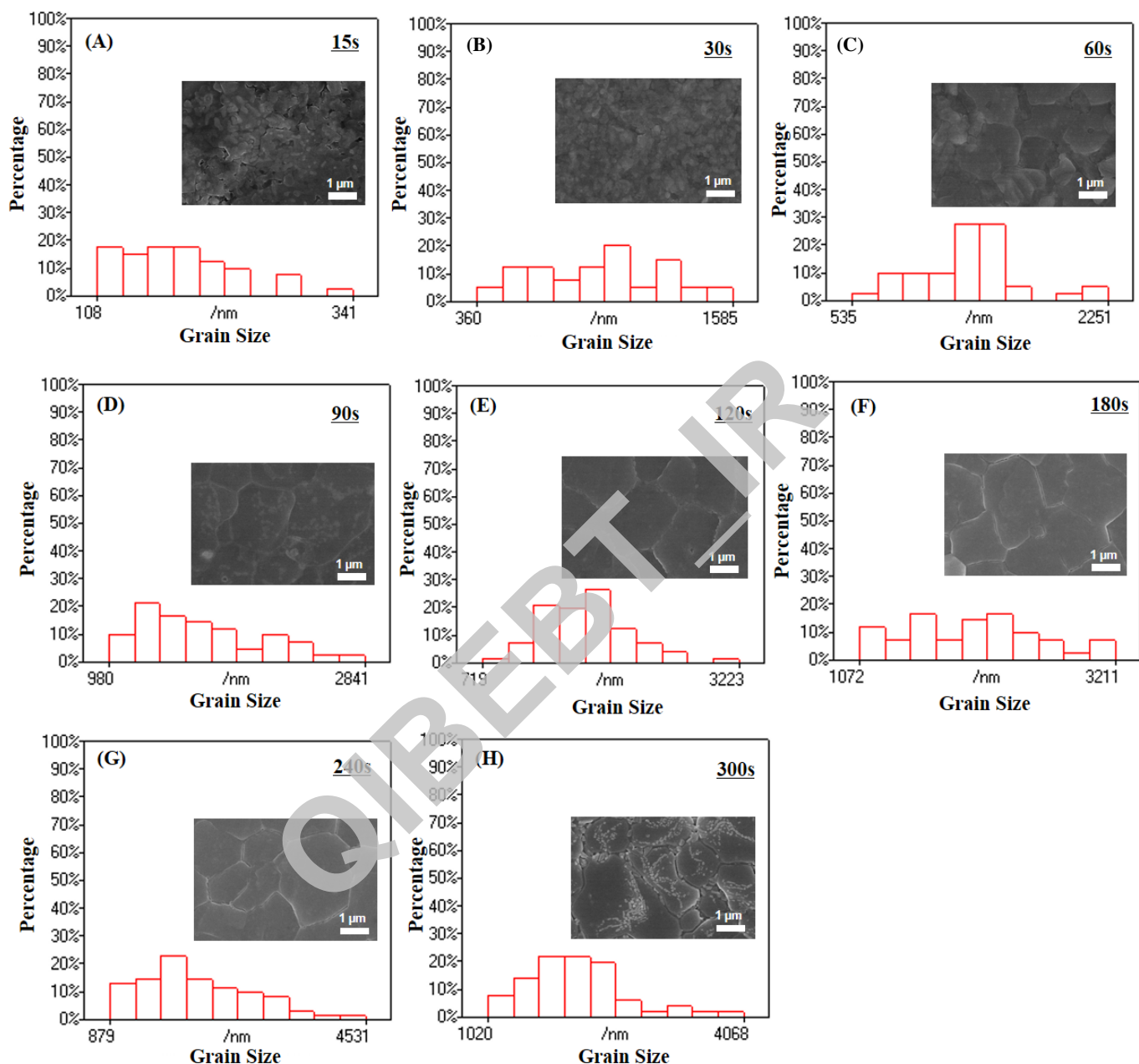


Figure S9. Grain size distributions of the RT-recrystallized MAPbI₃•MAcI thin film after thermal annealing at 150 °C for different durations: (A) 15 s; (B) 30 s; (C) 60 s; (D) 90s; (E) 120 s; (F) 180 s; (G) 240 s; (H) 300 s, based on image analyses of more than 40 grains each from the SEM images. Typical SEM images for the corresponding films are shown in the inset of each figures.

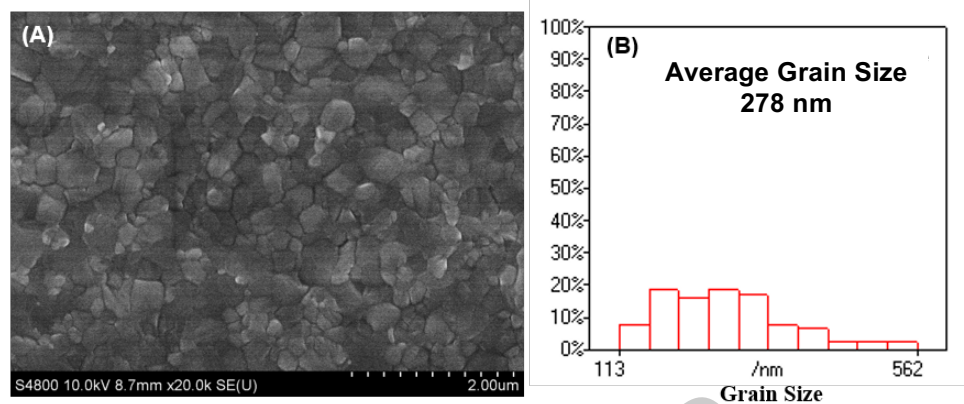


Figure S10. (A) SEM image (top surface) of the reference-MAPbI₃ thin film that is derived from MAPbI₃•xCH₃NH₂ (MAI-free). (B) Grain size distribution based on image analysis of SEM image in (A).

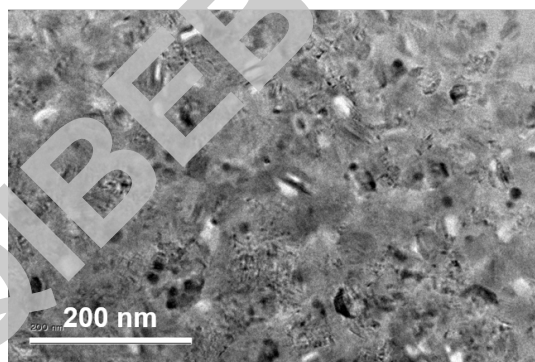


Figure S11. TEM image of the reference-MAPbI₃ thin film grown directly on a carbon-film-coated TEM grid from MAPbI₃•xCH₃NH₂ showing multiple layers of small grains.

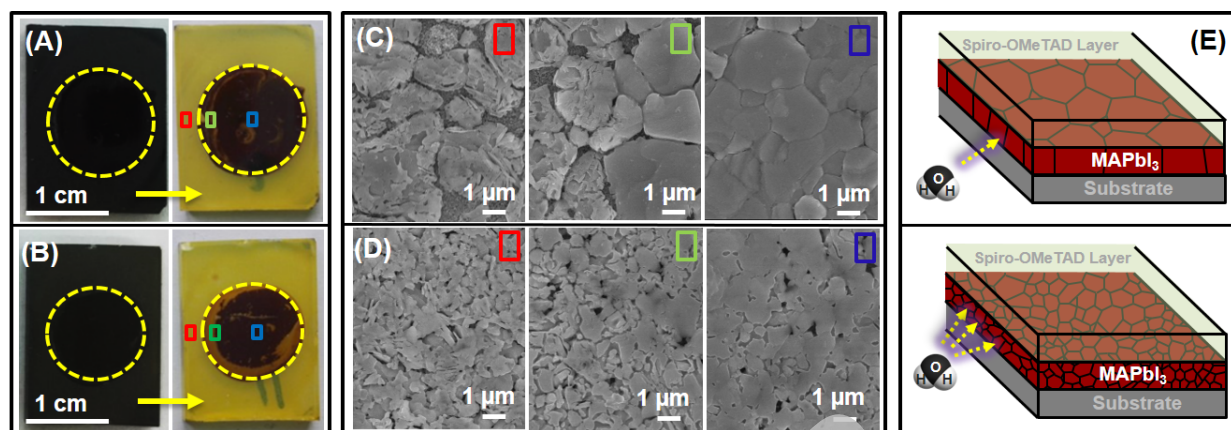


Figure S12. Photographs showing (A) the $\text{MAPbI}_3 \cdot \text{MACl} \cdot x\text{CH}_3\text{NH}_2$ -derived MAPbI_3 thin film (coarse-grained) and (B) the reference- MAPbI_3 thin film (fine-grained) after 96-h exposure to the ambient. The dashed circle indicates the area where a layer of Spiro-OMeTAD was deposited. (C, D) SEM images of regions marked in (A, B), respectively. (E) Schematic illustration of the beneficial role of the reduced GB density in the MAPbI_3 film on the ambient stability.

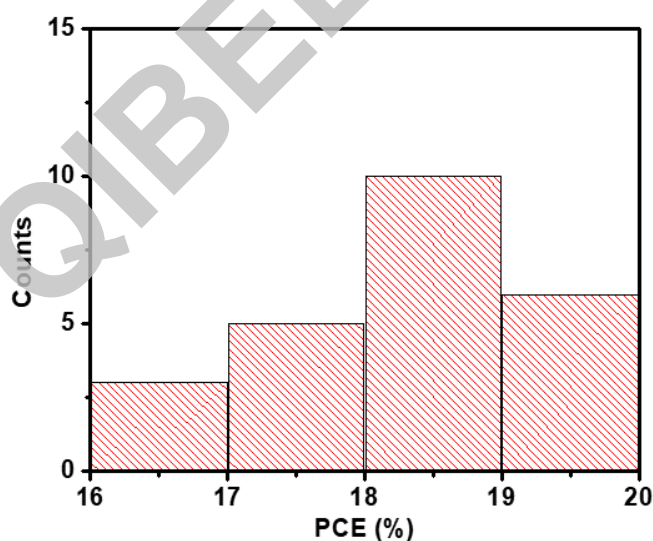


Figure S13. PCE statistics of PSCs made using the $\text{MAPbI}_3 \cdot \text{MACl} \cdot x\text{CH}_3\text{NH}_2$ -derived MAPbI_3 films.